

Supporting Information for Weighing nanoparticles in solution at the attogram scale

Selim Olcum^{a,b,1}, Nathan Cermak^{c,1}, Steven C. Wasserman^a, Kathleen S. Christine^{d,e}, Hiroshi Atsumi^f, Kristofor Payer^g, Wenjiang Shen^h, Jungchul Leeⁱ, Angela M. Belcher^{a,b,f}, Sangeeta N. Bhatia^{b,d,e,j,k}, Scott R. Manalis^{a,b,c,l,2}

^aDepartment of Biological Engineering, Massachusetts Institute of Technology, Cambridge, MA, 02139, USA

^bKoch Institute for Integrative Cancer Research, Massachusetts Institute of Technology, Cambridge, MA, 02139, USA.

^cComputational and Systems Biology Initiative, Massachusetts Institute of Technology, Cambridge, MA, 02139, USA

^dHarvard-MIT Health Sciences and Technology, Institute for Medical Engineering and Science, Massachusetts Institute of Technology, Cambridge, MA, 02139, USA

^eInstitute for Medical Engineering and Science, Massachusetts Institute of Technology, Cambridge, MA, 02139, USA

^fDepartment of Materials Science and Engineering, Massachusetts Institute of Technology, Cambridge, MA, 02139, USA

^gMicrosystems Technology Laboratories, Massachusetts Institute of Technology, Cambridge, MA, 02139 USA

^hInnovative Micro Technology, Santa Barbara, CA, 93117

ⁱDepartment of Mechanical Engineering, Sogang University, Seoul 121-742, Republic of Korea

^jDepartment of Electrical Engineering and Computer Science, Massachusetts Institute of Technology, Cambridge, MA, 02139, USA

^kHoward Hughes Medical Institute, Cambridge, Massachusetts 02139, USA

^lDepartment of Mechanical Engineering, Massachusetts Institute of Technology, Cambridge, MA, 02139, USA

¹ These authors contributed equally to this work.

Table of Contents

| | | |
|----|--|----|
| 1 | Device parameters..... | 2 |
| 2 | System operation..... | 2 |
| 3 | Detector noise..... | 4 |
| 4 | Thermal noise limit on Allan deviation..... | 7 |
| 5 | Limit of detection..... | 8 |
| 6 | Mass Sensitivity Calibration..... | 10 |
| 7 | Dynamic light scattering measurements of gold nanoparticles..... | 10 |
| 8 | Dynamic range in size..... | 11 |
| 9 | Accuracy of concentration estimation..... | 12 |
| 10 | Exosome diameter estimation..... | 14 |
| 11 | Dynamic light scattering measurements of exosomes..... | 14 |
| 12 | Repeated exosome measurements..... | 15 |
| 13 | Preparation of DNA covered gold nanoparticles..... | 16 |
| 14 | Design of DNA origami scaffold..... | 17 |
| 15 | Design and preparation of gold covered DNA origami..... | 18 |
| 16 | DNA sequence of staple strands..... | 19 |
| 17 | References..... | 20 |

1 Device parameters

| Type | Device ID | Frequency (kHz) | Q factor | $\delta f/\delta m$ (mHz/ag) |
|------|-----------|-----------------|----------|------------------------------|
| 0 | S1 | 517 | 22,000 | 0.95 |
| 0 | S3 | 545 | 14,000 | 0.95 |
| 0 | S4 | 590 | 17,000 | 0.99 |
| 0 | S6 | 577 | 24,000 | 1.08 |
| 1 | 4I | 1205 | 9,000 | 4 |
| 1 | 5B | 1240 | 12,000 | 4.9 |
| 1 | 8O | 973 | 9,500 | 3.4 |
| 1 | X4 | 1127 | 20,000 | 4 |
| 2 | X6 | 2493 | 20,000 | 14.3 |
| 2 | 13L | 1871 | 15,000 | 9.3 |
| 2 | 4K | 2201 | 16,000 | 9.1 |
| 2 | 11M | 1918 | 11,000 | 8.4 |
| 2 | 5J | 2214 | 18,000 | 10.5 |
| 2 | 5M | 2125 | 16,000 | 10.9 |
| 2 | 7A | 2873 | 15,000 | 14 |
| 3 | 8N | 2887 | 17,500 | 16 |
| 3 | 13M | 2662 | 15,000 | 14.2 |
| 3 | 4J | 3266 | 16,000 | 18 |
| 3 | 5N | 2079 | 17,000 | 14 |
| 3 | 7B | 3910 | 15,000 | 21.4 |

Table S1 Measured parameters of the cantilevers used in this study. The resonant frequencies and quality factors of the SNRs used in Figure 2 are measured by a lock-in amplifier (SRS-SR844) when the cantilevers are filled with ultra-pure deionized water. We measured the mass sensitivity of the cantilevers by weighing size-calibrated NIST traceable particles in each cantilever i.e. 30 nm gold (NIST SRM8012), 150 nm (Thermo Scientific 3150A), 200 nm (Thermo Scientific 3200A) and 220 nm (Thermo Scientific 3220A) polystyrene.

2 System operation

The cantilevers used in this work are operated in self-oscillation mode in a positive feedback loop. The image of the oscillator system is given in Fig. S1. The motion of the cantilever is converted to the deflection of a laser beam bounced off of the tip using an optical lever setup (Fig. 1a). We used an ultra-low noise diode lab laser module (Coherent 635 nm, 5 mW) as the laser source. We cleaned up and expanded the laser source by a spatial filter (0.5NA 13.86 mm aspherical lens, 20 μ m pinhole) and a collimating spherical lens ($f=30$ mm) to achieve a coherent ~ 3 mm-diameter filtered laser beam. Additionally, we used a film polarizer to tune the incident laser power on the cantilever. Increasing the laser power causes the temperature of the cantilever to fluctuate, which can be observed as frequency fluctuations of the oscillator. This is particularly the case for smaller cantilevers (Type 2 and 3). In all cases, we used the maximum laser power that can give the minimum frequency noise. The laser beam is focused on the cantilever tip using a 20X objective (Nikon LU Plan ELWD 0.4NA). The reflected laser beam is focused on the photodetector by an achromatic doublet lens (Thorlabs AC254-30-A). The spot size on the photodetector is adjusted by changing the distance of the focusing lens to the photodetector.

Supporting Information for “Weighing nanoparticles in solution at the attogram scale”

We used a custom-made low-noise photodetector circuit to transform the angular deflection acquired from the optical lever setup to an electrical signal by a high-speed split PIN photo-diode (Hamamatsu S4204). We used ultra-low-noise transimpedance amplifiers (OPA847) with 5 MHz 3 dB-bandwidth followed by a high speed instrumentation amplifier (AD8130) to convert the differential optical deflection signal on the split photodiode to a voltage signal. The generated voltage signal is amplified by an automatic gain control (AGC) stage to achieve constant amplitude at the output of the photodetector. The output amplitude can be tuned by a DC input voltage connected to the AGC stage.

The optimal delay required in the loop for stable self-oscillation is introduced by a field programmable gate array (FPGA, Altera Cyclone IV on DE2-115). The analog signal in the loop is interfaced with the digital signal in the FPGA using the Terasic AD/DA conversion board at 100 MSPS with 14-bit converters. The FPGA and the conversion board run on an external 100 MHz oven controlled crystal oscillator clock (Abracon AOCJY2-E-H1C). The delay algorithm in the FPGA is capable of achieving sub-clock delays (39 ps minimum) using numerical interpolation, which converts to less than 0.1 degree resolution for adjusting the phase shift of

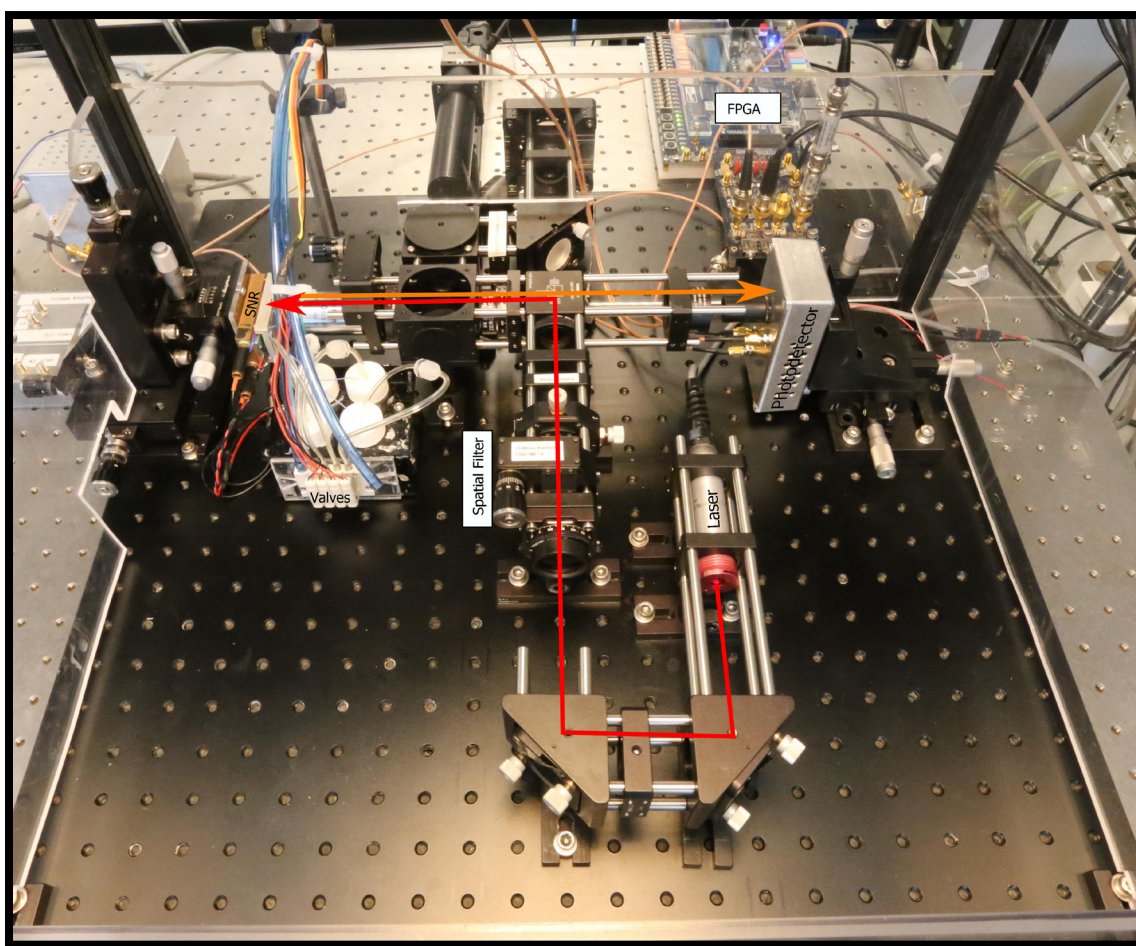


Figure S1 Photograph of the oscillator system. The incident laser path onto the cantilever is indicated with a red line. The orange line shows the reflected laser path from the cantilever.

the highest frequency oscillators used in this work (4 MHz).

Since the amplitude of photodetector output is kept constant by the AGC, the oscillation amplitude of a cantilever can be adjusted by the FPGA independently. The output of the FPGA is amplified with a gain of 15 dB using an amplifier utilizing a high current OPAMP (LT1210) output stage, which drives a piezoceramic actuator (American Piezo Co. APC841, 7x7x0.2 mm) integrated underneath the SNR chip.

The frequency of oscillation is measured by period counting at 100 MHz using a digital heterodyne mixer and a low-pass filter coded in the FPGA. The signal is mixed with a reference sinusoid generated by a numerically-controlled oscillator (NCO). The heterodyned signal is then filtered using a 3-stage cascaded integrator comb (CIC) filter with a width of 500 data points (5 μ s) and then up-sampled (1st-order hold) back to 100 MHz. The number of clock cycles in between zero crossings of the resulting signal is counted to infer the period. Note that the difference of the reference frequency and the oscillation frequency determines the RF measurement bandwidth.

The FPGA communicates with a control computer via Ethernet. The computer is used to control the delay in the loop and the amplitude of oscillation as well as the bandwidth of the frequency measurement algorithm. Measured oscillation frequency waveform (baseband signal) is recorded by the control computer for post-processing.

3 Detector noise

For performing an analysis on the noise sources limiting the noise performance of the SNRs, we first measured the voltage noise power spectrum density of the photodetector output, S_V^{pd} (V^2/Hz) in our optical lever setup using a spectrum analyzer (HP 4395A) when the water-filled cantilevers were driven only by the thermal energy due to the non-zero ambient temperature, T ($\sim 300K$). The displacement noise spectral density of a cantilever due to thermal energy, S_x^{th} (m^2/Hz) as a function of frequency, ω is given by(1):

$$S_x^{th}(\omega) = \frac{4\omega_0^3 k_B T}{kQ} \frac{1}{(\omega_0^2 - \omega^2)^2 + (\omega\omega_0/Q)^2} \quad (1)$$

where, k_B , k , Q and ω_0 are Boltzmann constant and stiffness, quality factor and resonant frequency of the cantilever. At the resonant frequency, above equation reduces to $4k_B T Q / \omega_0 k$, which can be used to calculate the responsivity (V/m) of the optical lever setup as follows:

$$R = \sqrt{\frac{S_V^{pd}(\omega_0) - S_V^{pd}(\omega \neq \omega_0)}{S_x^{th}(\omega_0)}} = \sqrt{\frac{S_V^{pd}(\omega_0) - S_V^{pd}(\omega \neq \omega_0)}{4k_B T Q / \omega_0 k}} \quad (2)$$

For calculating the responsivity of the optical lever setup we used the measured parameters of the cantilever under test. The resonant frequencies and the quality factors are given in Table S1. The stiffness of a cantilever is calculated using the measured mass sensitivity values in the same table using the following relation:

$$\frac{\delta f}{\delta m} = -\frac{f_0}{2m^*} = -\frac{2\pi^2 f_0^3}{k} \quad (3)$$

where m^* is the effective mass of the cantilever. Using the above relations and measured cantilever parameters, we calculated the displacement noise power spectral density for different types of SNRs used in this work. The results are given in Figure S2. The red circles are

the spectrum analyzer (HP 4395A) measurements referred to displacement domain performed at 3 Hz resolution bandwidth with 100 averages. The dashed black curves are calculated using equation (1) and the dashed green lines are the calculated noise density of the photodetector referred to the displacement domain. We measured the photodetector noise floor between $90\text{-}140\text{ fm}/\sqrt{\text{Hz}}$ for all types of cantilevers. The noise of the optical lever setup is limited by the thermomechanical vibrations of the cantilevers at the vicinity of their resonant frequencies and by the photodetector noise floor at frequencies away from the resonant frequency.

For investigating the effect of the displacement noise on the oscillator performance we measured the root-mean-square (RMS) frequency noise of the cantilevers when they were oscillating in feedback. We then compared the acquired noise measurements to the RMS frequency noise due to thermal energy and detector noise, which can be calculated following the analysis given by Albrecht et al.(1) as:

$$\langle \delta\omega^2 \rangle = \frac{k_B T}{k \langle x_c^2 \rangle} \frac{\omega_0 B}{Q} + \frac{B^3 S_x^{pd}}{12 \langle x_c^2 \rangle} \quad (4)$$

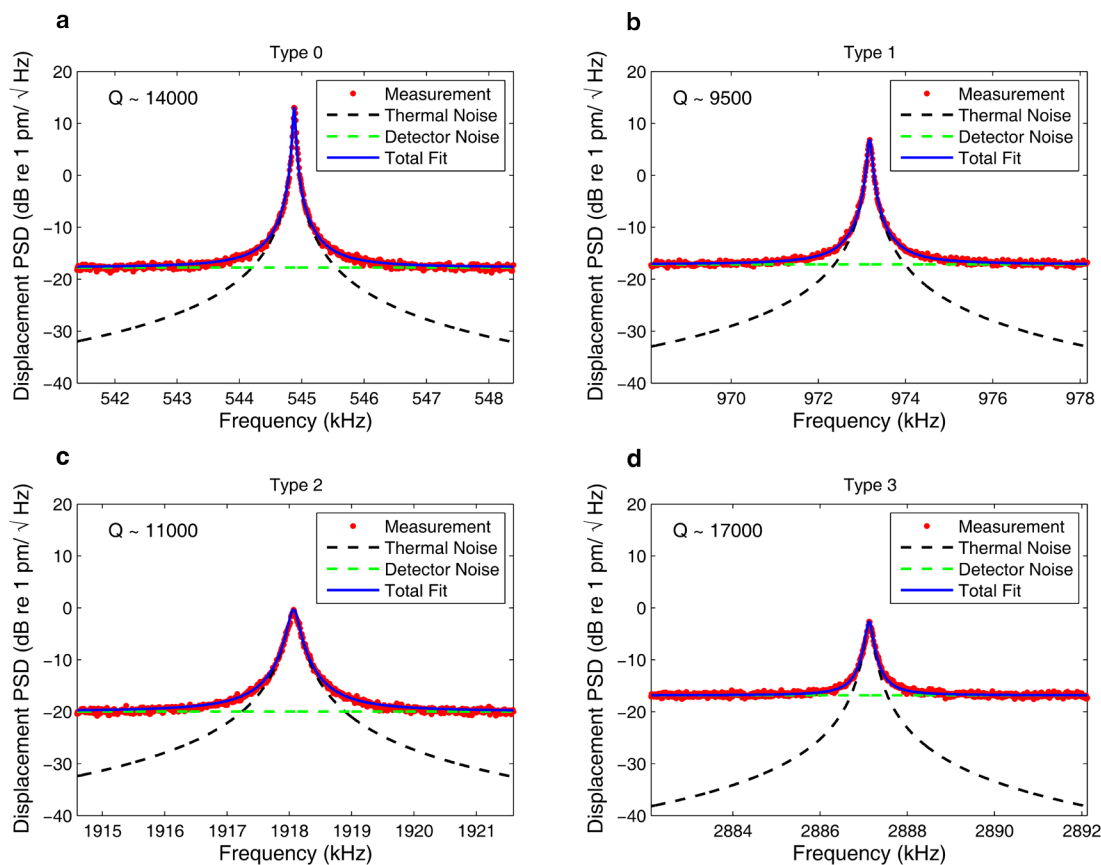


Figure S2 Displacement noise density of SNRs of different types. The red circles are calculated by referring the measured voltage power spectral density of the cantilevers due to thermal vibrations to displacement domain. The dashed black lines are the calculated displacement noise density of the cantilevers due to thermal vibrations using equation (1). The green dashed lines are the calculated displacement noise floor of the photodetector. The spectrum measurements are performed using 3 Hz resolution bandwidth and 100 averages.

where B is the RF measurement bandwidth, S_x^{pd} is the photodetector power spectral density referred to the displacement domain in m^2/Hz and $\langle x_c \rangle$ is the RMS displacement of the cantilever tip. The first term in this equation is due to the thermal energy and the second term is due to the photodetector noise. The RMS displacements of the cantilevers used in this work are limited by the mechanical nonlinearity. We used the approximate displacement expression given by Arlett et al.(2) converted to RMS at the onset of nonlinearity as

$$\langle x_c \rangle = 5.46 \frac{L}{\sqrt{2Q}} \quad (5)$$

where L is the length of the cantilever. The calculated RMS noise values as a function of measurement bandwidth are given in Figure S3. The red dots are the measured RMS frequency noise in 1 second intervals as a function of measurement bandwidth and when the cantilevers are in self-oscillation at their onset of nonlinearity. The dashed black lines are the estimated noise due to the thermal energy and the black solid curves are the estimated noise due to the combination of thermal energy and the photodetector noise as given in equation (4).

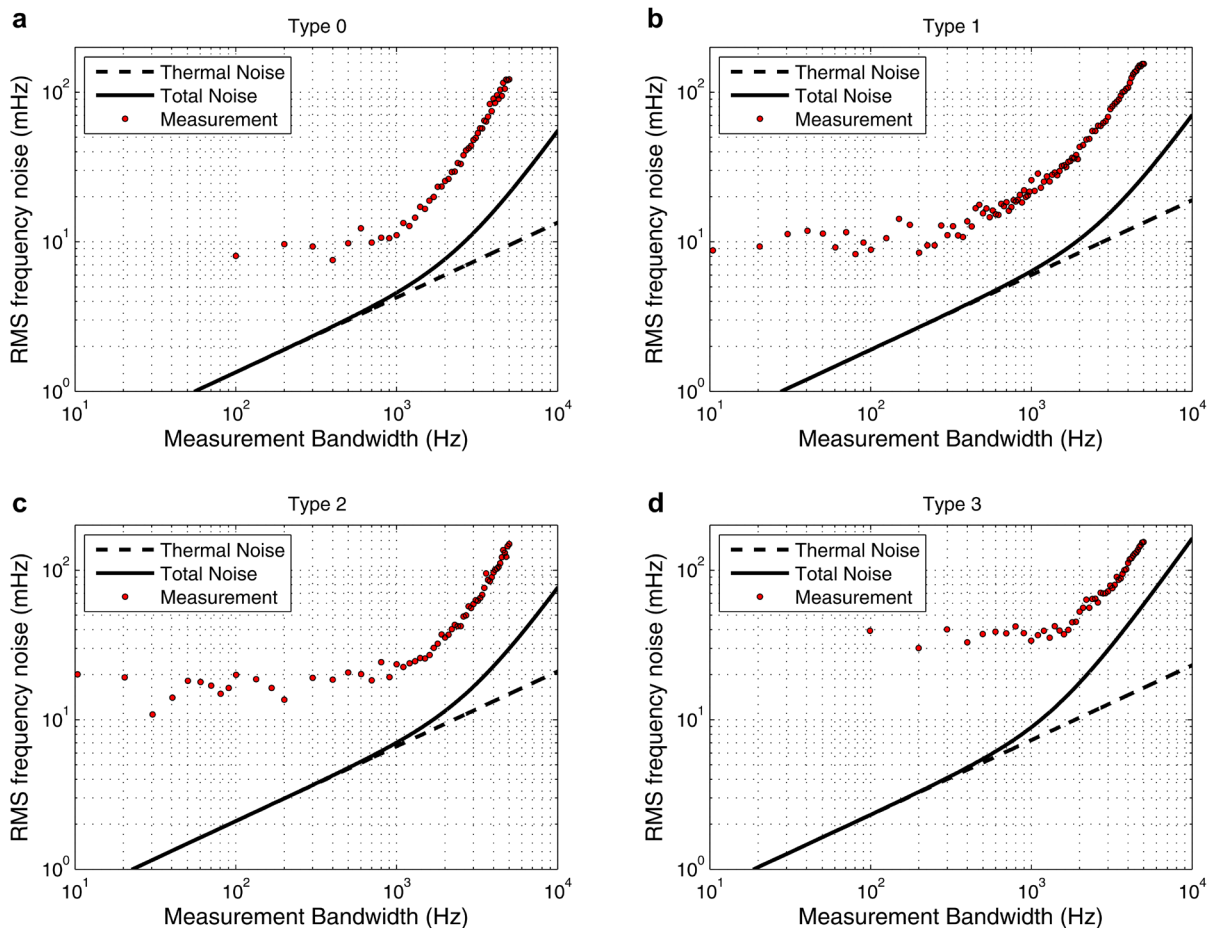


Figure S3 Root-mean-square frequency noise of the oscillators are measured as a function of measurement bandwidth for different types of SNRs and plotted as red circles. The dashed black lines are the RMS frequency noise due to thermal energy calculated using the first term in equation (4). The solid black lines are the calculated RMS noise due to the detector noise floor and thermal energy. Each red circle is calculated using 1 second of frequency noise measurement.

From Figure S3, we can see that all types of cantilevers are limited by the photodetector noise at wide measurement bandwidths. Increased noise at wide measurement bandwidth limits the throughput for better mass resolution cases. Approximately flat RMS frequency noise at narrower bandwidth operation is also observed in Allan deviation curves in Fig. 2 as the flicker noise region. Especially for device types 2 and 3, if the displacement noise floor of the motion detector can be reduced, the throughput of the device can be increased up to 10-fold without sacrificing mass resolution.

4 Thermal noise limit on Allan deviation

In order to calculate the fundamental noise limit on frequency stability in terms of Allan deviation due to the thermal noise on the cantilever, we treat the cantilever as a damped harmonic oscillator. The spectral density of the random displacements of the cantilever, $S_x^{th}(\omega)$ was given in equation (1), which is used here to calculate the spectral density of the phase fluctuations, $S_\varphi^{th}(\omega)$:

$$S_\varphi^{th}(\omega) = \frac{S_x^{th}(\omega)}{\langle x_c \rangle^2} = \frac{4\omega_0^3 k_B T}{k \langle x_c \rangle^2 Q} \frac{1}{(\omega_0^2 - \omega^2)^2 + (\omega\omega_0/Q)^2} \quad (6)$$

Equation (6) can be approximated as follows (1) for very high Q oscillators:

$$S_\varphi^{th}(\omega) \approx \frac{\omega_0 k_B T}{k \langle x_c \rangle^2 Q} \frac{1}{(\omega - \omega_0)^2} \quad (7)$$

If we convert the above relation to baseband around the carrier frequency ω_0 by defining a modulation frequency $\omega_m = \omega - \omega_0$, we get the phase noise density as:

$$S_\varphi^{th}(\omega_m) \approx \frac{\omega_0 k_B T}{k \langle x_c \rangle^2 Q} \frac{1}{\omega_m^2} = \frac{\omega_0 k_B T}{E_C Q} \frac{1}{\omega_m^2} \quad (8)$$

where E_C is the carrier energy defined as $k \langle x_c \rangle^2$. The Allan variance due to the phase noise density of an oscillator is calculated using the following relation (3):

$$\sigma_A^2(\tau) = 2 \left(\frac{2}{\omega_0 \tau} \right)^2 \int_0^\infty S_\varphi(\omega) \sin^4(\omega\tau/2) d\omega \quad (9)$$

If we evaluate the integral above using the phase noise density in equation (8), we get:

$$\sigma_A^{th}(\tau) = \sqrt{\frac{\pi k_B T}{\tau E_C Q \omega_0}} = \sqrt{\frac{k_B T}{2 \tau E_C Q f_0}} \quad (10)$$

Since the cantilevers in this work are driven at their onsets of nonlinearity, we use the approximate expression given in equation (5) as the RMS displacement to calculate the nonlinearity limited Allan deviation due to thermal noise,

$$\sigma_{A,non}^{th}(\tau) = \frac{1}{5.46L} \sqrt{\frac{k_B T}{\tau k f_0}} \quad (11)$$

which is independent of the quality factor. Therefore, as long as an oscillator is driven at its onset of nonlinearity, the lowest Allan deviation that can be achieved does not depend on the quality factor of the resonator. In that case the practically achievable stability would be limited by the coupling efficiency of the actuator or the power handling capability of the resonator. The fundamental limits on the Allan deviation of the oscillators used in this work, which are plotted

in Figure 2 of the manuscript as a function of gate time, τ , are calculated using equation (11) and the design parameters given in Table 1 of the manuscript.

5 Limit of detection

We calculated limits of mass detection of the SNRs by taking measurements of instrument noise (the same data as used for Fig. 2), filtering with an FIR filter, h_T , and calculating the standard deviation, σ_T of the remaining signal, illustrated in Figure S4. The filter h_T was defined as the peak shape given in Dohn et al.(4) for a peak of width T , with the mean subtracted and then the amplitude normalized such that the gain for a peak of the same width was unity. This approach deviates slightly from the truly optimal (in terms of signal-to-noise ratio) FIR filter for detecting a signal s , which is given by

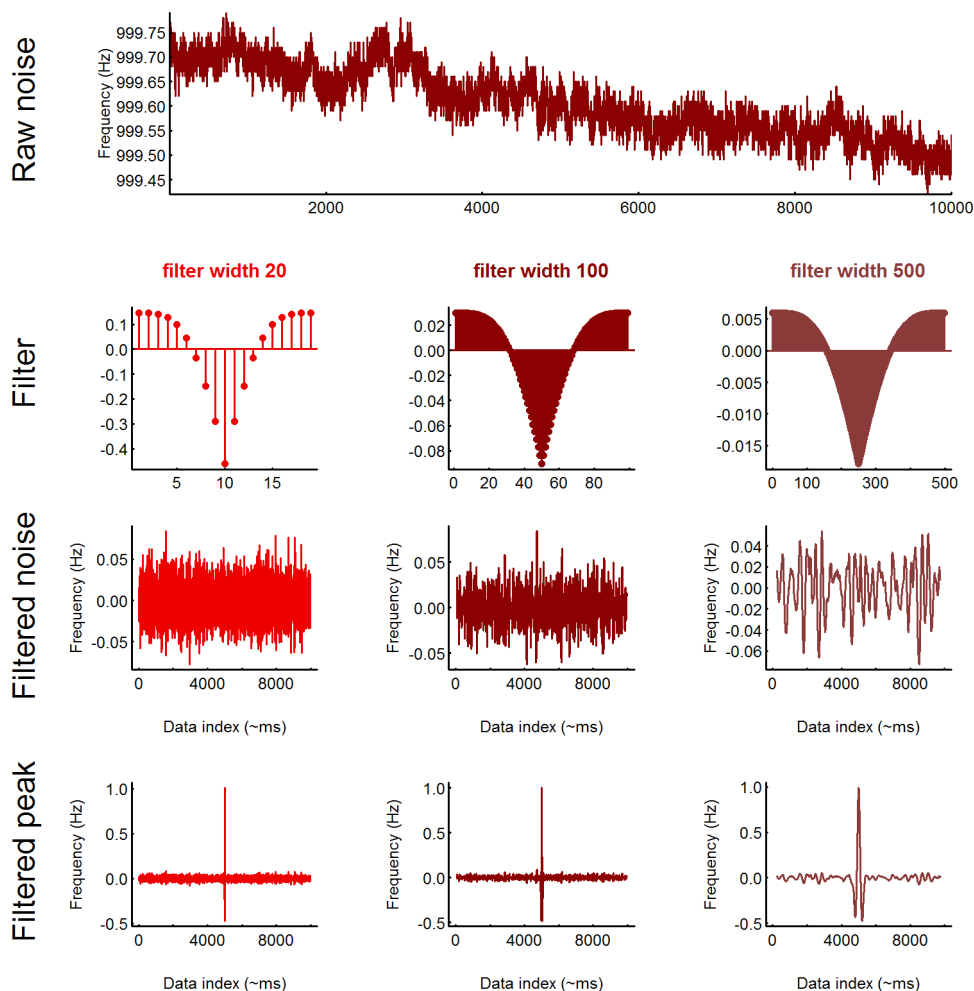


Figure S4 Illustration of the method used for calculating limits of detection using matched filters of varying peak widths. Raw noise is filtered with a filter shaped like the signal generated by a particle transiting the cantilever, with the mean subtracted. The filters are normalized such that a 1 Hz peak input yields a 1 Hz peak out.

$$h = \alpha R^{-1}s \quad (12)$$

where h is the vector of filter coefficients (taps), α is a normalization constant, and R is the covariance matrix of the noise. Because our noise has long correlation times (a defining characteristic of $1/f$ and $1/f^2$ noise) leading to extremely long optimal FIR filters, instead of multiplying our signal by R^{-1} , we approximate the true matched filter by simply subtracting off the mean (DC component) of our peak shape (shown in second row of Figure S4). This effectively includes a high-pass component in our filter that should reject frequencies below those in our peak. After filtering, we calculate the standard deviation σ of the resulting signal, and define our limit of detection as 3σ , shown in Figure S5.

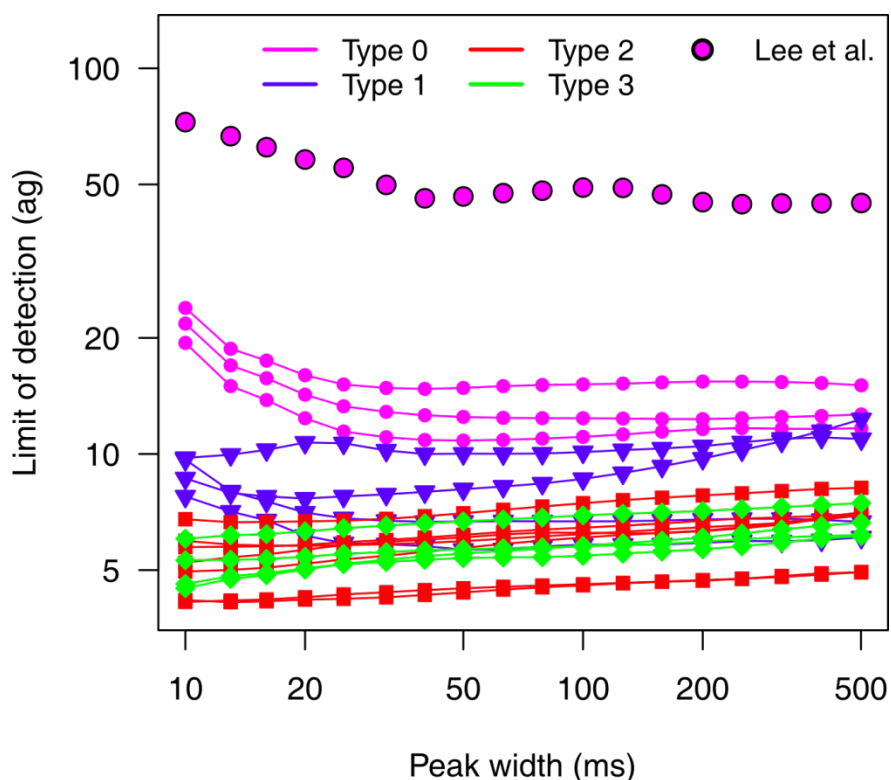


Figure S5 Limits of mass detection for the devices considered in this study. Limits of detection are calculated based on applying approximately matched filters of varying widths and calculating three times the resulting noise standard deviation. The apparent independence of limit of detection and peak width over the range from 20-500 mHz results from the dominating $1/f$ noise, which has equal power in every decade of the spectrum.

6 Mass Sensitivity Calibration

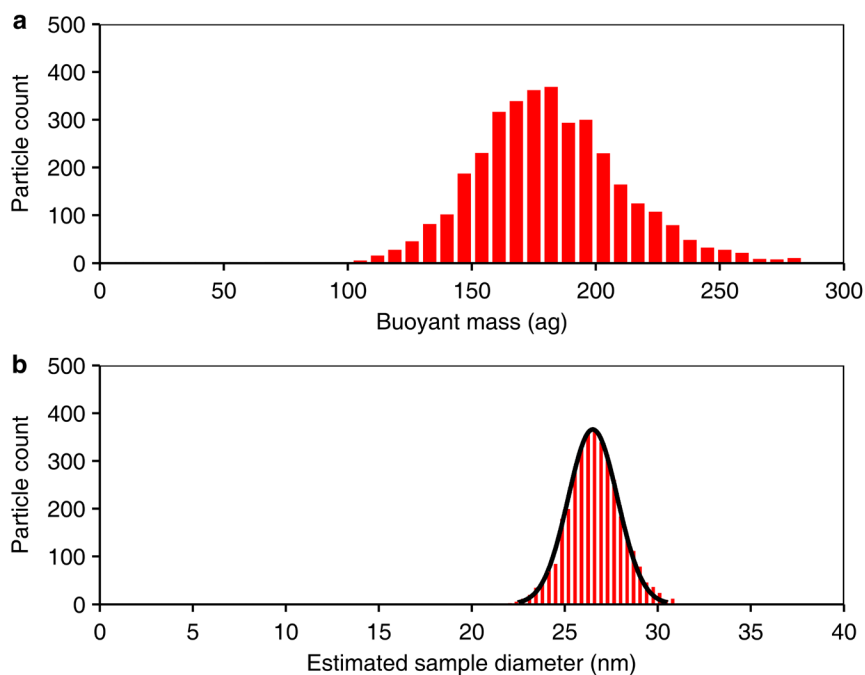


Figure S6 Mass sensitivity calibration of SNRs. We calibrated the mass sensitivity of the cantilevers by running gold nanoparticles (RM-8012, NIST) as reference before the actual experiment. We calculate the sensitivity of a cantilever such that the mean diameter of the measurement is 26.5 nm, which is the mean of the estimated diameter of the nanoparticles by AFM, SEM and TEM measurements in the reference material datasheet. **(a)** Buoyant mass histogram of reference gold nanoparticles. 3,600 particles are measured in a 20-minute experiment. **(b)** Histogram of the estimated diameter of weighed particles by assuming a spherical shape and uniform gold density of 19.3 g/cm^3 .

7 Dynamic light scattering measurements of gold nanoparticles

For comparing the performance of SNRs to dynamic light scattering (DLS), we measured the gold nanoparticle populations used in the experiment given in Fig. 3 using a Malvern ZEN3690 DLS instrument. First, we analyzed 10 nm, 15 nm and 20 nm gold nanoparticles, separately. The results of the measurements are given in Table S2, below.

| Sample | DLS | | SNR (from the mixture) | | Datasheet | |
|----------------|-----------|-------|------------------------|-------|-----------|-------|
| | Mean (nm) | CV(%) | Mean (nm) | CV(%) | Mean (nm) | CV(%) |
| 1 10 nm AuNP | 12.68 | 10.2 | 9.9 | 7.4 | 9.9 | |
| 2 15 nm AuNP | 15.99 | 13.4 | 14.4 | 5.3 | 14.3 | < 8% |
| 3 20 nm AuNP | 22.07 | 15.6 | 19.7 | 4.9 | 20.4 | < 8% |
| 4 Mixture | 18.77 | 24.8 | | | | |

Table S2 DLS measurements of the gold nanoparticles used in this work. Samples 1, 2 and 3 are monodisperse populations of gold nanoparticles used in sample 4, which was weighed in the SNR and the results were given in Fig. 3.

For the mono-disperse gold nanoparticle populations, the mean diameters measured by the DLS are slightly higher than what were measured by SNR or reported in the datasheets of the particles. The measured coefficients of variances (CV's) by the DLS are also higher than SNR measurements. More importantly, DLS detects the mixture of these particles as a single peak around 18.77 nm with a relatively broader coefficient of variance (24.8%) compared to the single particle measurements.

8 Dynamic range in size

We demonstrate the dynamic range of SNRs by weighing a mixture of equal concentration 150 nm, 200 nm and 220 nm polystyrene beads (NIST traceable Thermo Scientific). The same cantilever and detection and estimation parameters that were used for gold nanoparticle mixture that was shown in Fig. 3 were used to weigh the polystyrene nanoparticle mixture. The three populations were successfully identified by measuring more than 12,500 particles in less than 30 minutes. We estimated the average transit time for a single particle as 30 ms. The estimated diameters in Figure S7b is calculated by assuming a spherical shape and uniform polystyrene density of 1.05 g/cm^3 . Calculated coefficient of variations and the mean sizes for the three populations are 2.3% around 149.8nm, 1.7% around 199.9nm and 1.2% around 217.2nm, respectively.

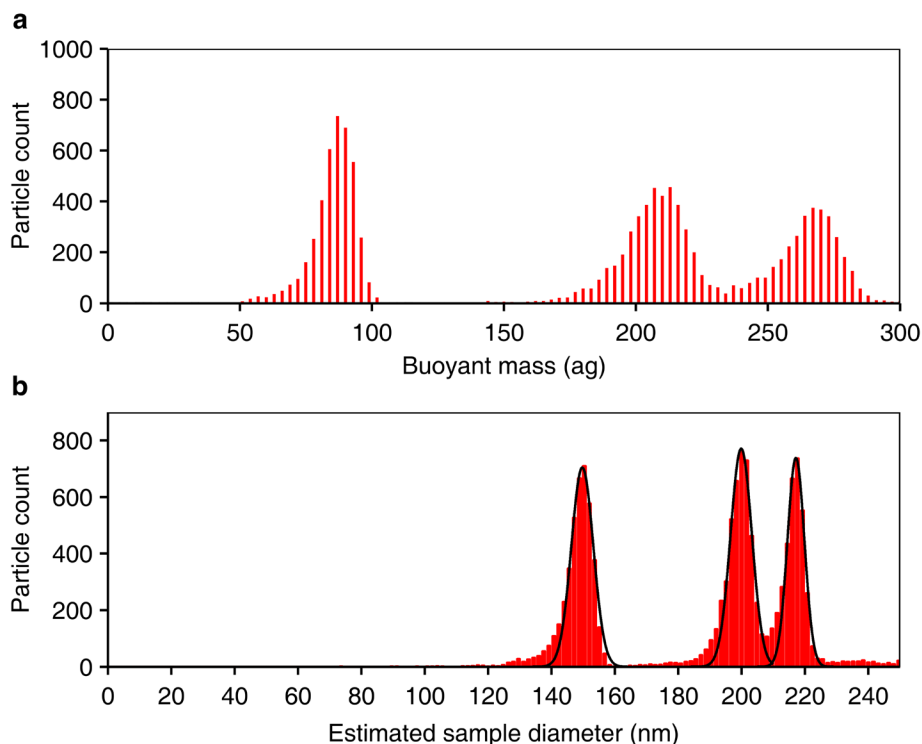


Figure S7 Dynamic range of SNRs. (a) Buoyant mass histogram of a mixed population of 150 nm, 200 nm and 220 nm polystyrene nanoparticles. **(b)** Estimated diameters of weighed nanoparticles. Black curves are Gaussian fits to the histograms.

9 Accuracy of concentration estimation

The concentration of particles in a solution is estimated by the ratio of the number of particles detected and the estimated total analyte volume. The amount of analyte flowing through the cantilever is calculated using the transit time estimates of the particles and the cantilever dimensions. Concentration accuracy is affected by the error in the particle count and the error in the estimated analyte volume.

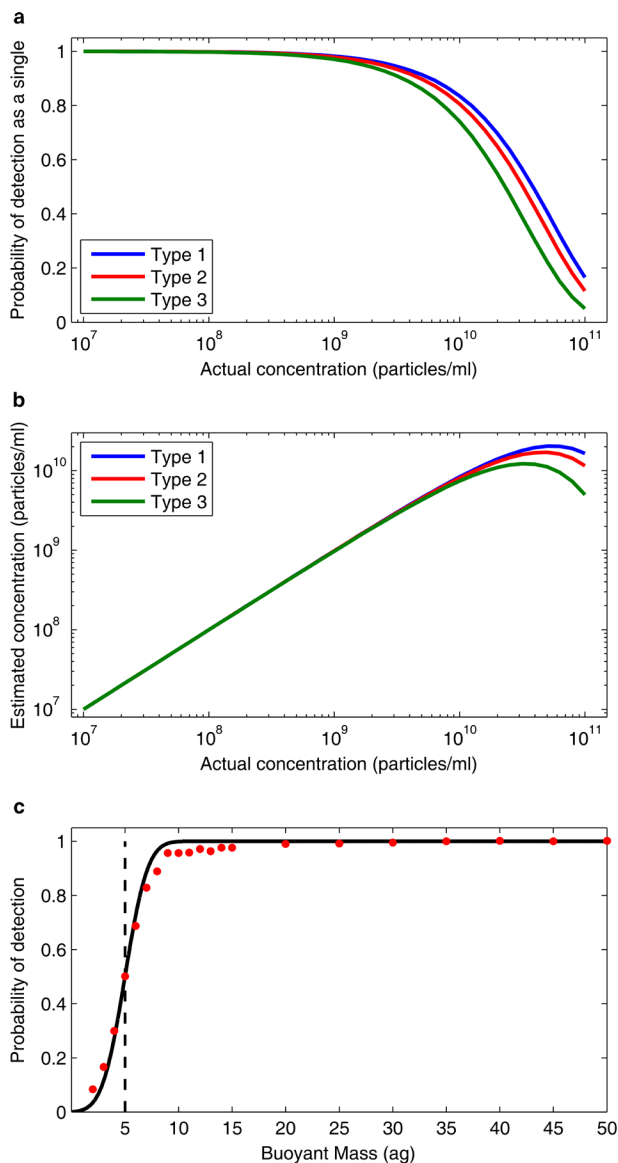


Figure S8 Accuracy of the concentration estimates. (a) Probability of a particle being detected (vs being coincident with another particle) as a function of sample concentration. **(b)** Estimated concentration as a function of actual concentration when there are no other error sources. **(c)** Probability of detection of a particle as a function of buoyant mass. The vertical dashed line is the limit of detection (5 ag) for the cantilever under consideration. The red circles are the simulation results using the detection algorithm when simulated particle peaks are inserted in real frequency noise data.

Erroneous particle counts are caused by two primary factors – coincident (overlapping) particles in the cantilever, and failure to detect particles that are close to the limit of detection. Coincidence occurs if two particles transit the cantilever close together enough that they cannot be distinguished from a single, larger particle. Here, we conservatively consider particles to be coincident if the distance between two particles in the cantilever channel is less than half the cantilever length. Using the channel dimensions and assuming particle arrival follows a Poisson process, we calculate the probability of any given particle being sufficiently spaced from its neighbors to be detected, as a function of the particle concentration (Figure S8a). This allows us to predict the relationship between actual and observed concentrations (Figure S8b). For Type 3 devices, the error in the concentration estimate of a sample with 10^{10} particles/ml is about 15%, and is higher for the longer devices.

Another contribution to the particle count error comes from the probability of detecting a particle passing through the buried channel. The probability of detection of a particle with a buoyant mass at the detection threshold given in Figure S5 is 50% due to the inherent noise of the system. We calculated the probability of detection as a function of particle buoyant mass by integrating the frequency noise distribution converted to mass around the limit of detection. For a cantilever with 5 ag limit of detection, the probability of detection as a function of the buoyant mass is given in Figure S8c. The solid line is the calculated theoretical detection probability whereas the red circles are the results of the detection of simulated particle signals superimposed on a measured noise waveform. A total of 600 particles were injected in the measured noise waveform of 10 minutes and the detection algorithm was used to detect the superimposed particle signals. The simulation results and the theoretical estimations agree well.

Estimating the flow rate of the fluid passing through the buried channel using the pressure difference across the cantilever and the channel dimensions does not provide satisfactory results since the flow rate during an experiment may vary due to partial clogging or surface adhesion. So we use the particle transit time through the cantilever as an estimate of the linear flow velocity. Coupled with the cantilever dimensions, we can use this to estimate the volumetric flow rate. To assess the accuracy of this method, we simulate the performance of our detection algorithm on estimating the transit time of the particles. We inject 600 particles with 100 ms transit time to a measured frequency noise waveform of Type 2 device with 5 ag limit of detection. As expected, the variance of the transit time estimates increases as the particle mass approaches to the limit of detection. We calculated the standard deviation of the transit time estimates as 20.5 ms around a mean of 95.2 ms for 10 ag particles. Although individual particles show a large variance the error on the mean value for 600 particles is less than 5% and gets smaller for higher number of measured particles. The variance of the transit time estimates reduces very quickly as the signal to noise ratio improves. For example, the error of transit time estimate using 100 ag particles (600 particles) is less than 1% with a standard deviation of 1.8 ms.

10 Exosome diameter estimation

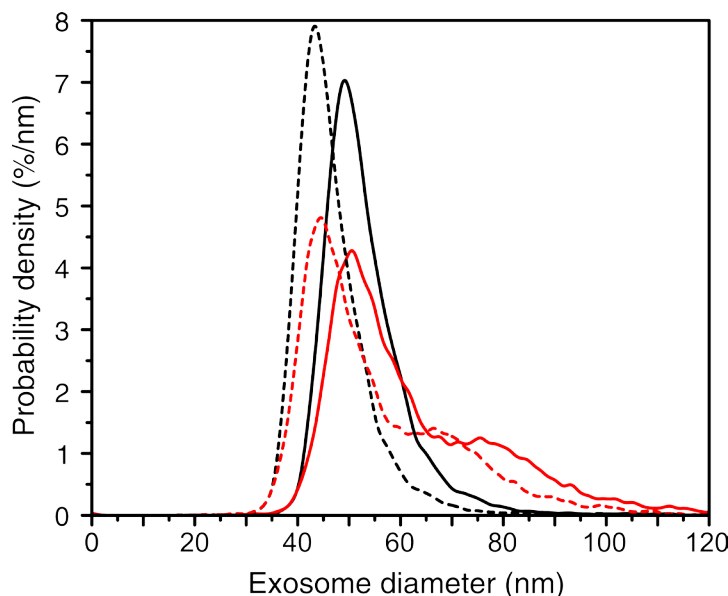


Figure S9 Estimated size distribution (kernel density estimates) of fibroblast (red) and hepatocyte (black) exosomes for different assumed exosome densities. The data used for size estimation is the buoyant mass measurements in Fig. 4. Two extreme cases for the mean exosome density are considered; 1.13 g/ml (solid), and 1.19 g/ml (dashed). All exosomes are assumed to be spherical.

11 Dynamic light scattering measurements of exosomes

We performed DLS measurements of different types of exosome populations for comparison. The mean of the dominant mode (in concentration) detected by the DLS is 44.6 nm and 44.1 nm for fibroblast and hepatocyte exosomes with standard deviations of 12.9 nm and 6.3 nm, respectively. The DLS measurements, similar to SNR measurements, estimate a broader distribution for the fibroblast exosomes compared to hepatocyte exosomes. However, DLS does not provide information about the shape of the distribution or absolute concentration. In addition, we note that the information gathered from the DLS is not very reliable for heterogeneous samples like exosomes, due to the fact that DLS is biased towards the detection of larger particles (5).

| Exosomes | | DLS | |
|----------|------------|-----------|----------|
| | | Mean (nm) | Std (nm) |
| 1 | Fibroblast | 44.6 | 12.9 |
| 2 | Hepatocyte | 44.1 | 6.3 |

Table S3 DLS measurements of the exosome populations analyzed in this work. Malvern ZEN3690 DLS instrument is used for the measurements.

12 Repeated exosome measurements

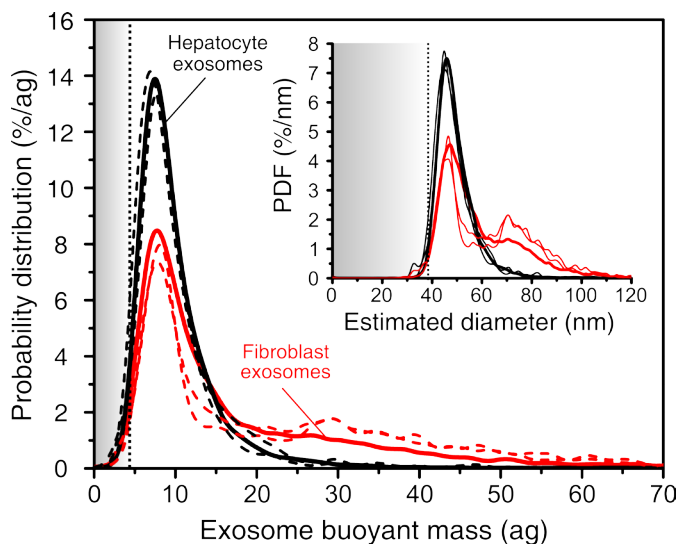


Figure S10 Distribution of buoyant mass measurements (kernel density estimates) of exosomal vesicles derived from fibroblast (red) and hepatocyte (black) cells. The thinner dashed lines are the results of the repeated measurements using a second batch of purified fibroblast and hepatocyte exosomes and using a different cantilever. The vertical line close to 5 ag depicts the limit of detection of the measurements. The inset shows the estimation of exosome diameter by assuming a spherical shape and uniform density of 1.16 g/ml.

13 Preparation of DNA covered gold nanoparticles

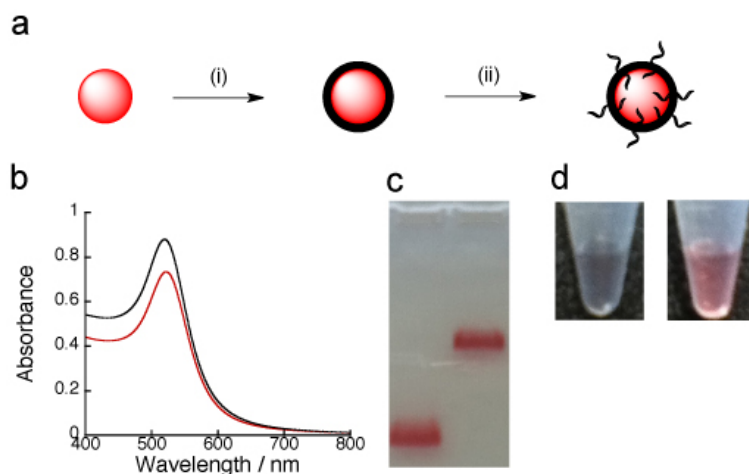


Figure S11 Preparation of DNA-covered gold nanoparticle. (a) Schematic illustration of a DNA-covered gold nanoparticle. (i) Gold nanoparticles were incubated with bis(*p*-sulfonatophenyl)-phenylphosphine (BSPP) at room temperature overnight. (ii) The phosphinated gold nanoparticle solution was incubated with activated thiol-DNA at room temperature overnight. (b) UV spectra of a bare gold nanoparticle (black, $\lambda_{\max} = 519.5$ nm) and a phosphinated gold nanoparticle (red, $\lambda_{\max} = 522.5$ nm). Phosphination of a gold nanoparticle causes the change of environment on its surface and λ_{\max} of the phosphinated gold nanoparticle shifts by 3 nm. (c) Agarose gel analysis identifies phosphinated (left) and DNA-covered (right) gold nanoparticles. (d) A photograph of phosphinated gold nanoparticles (left) and DNA-covered gold nanoparticles (right) under high salt conditions. Gold nanoparticles not covered by DNA aggregate under high salt solution.

14 Design of DNA origami scaffold

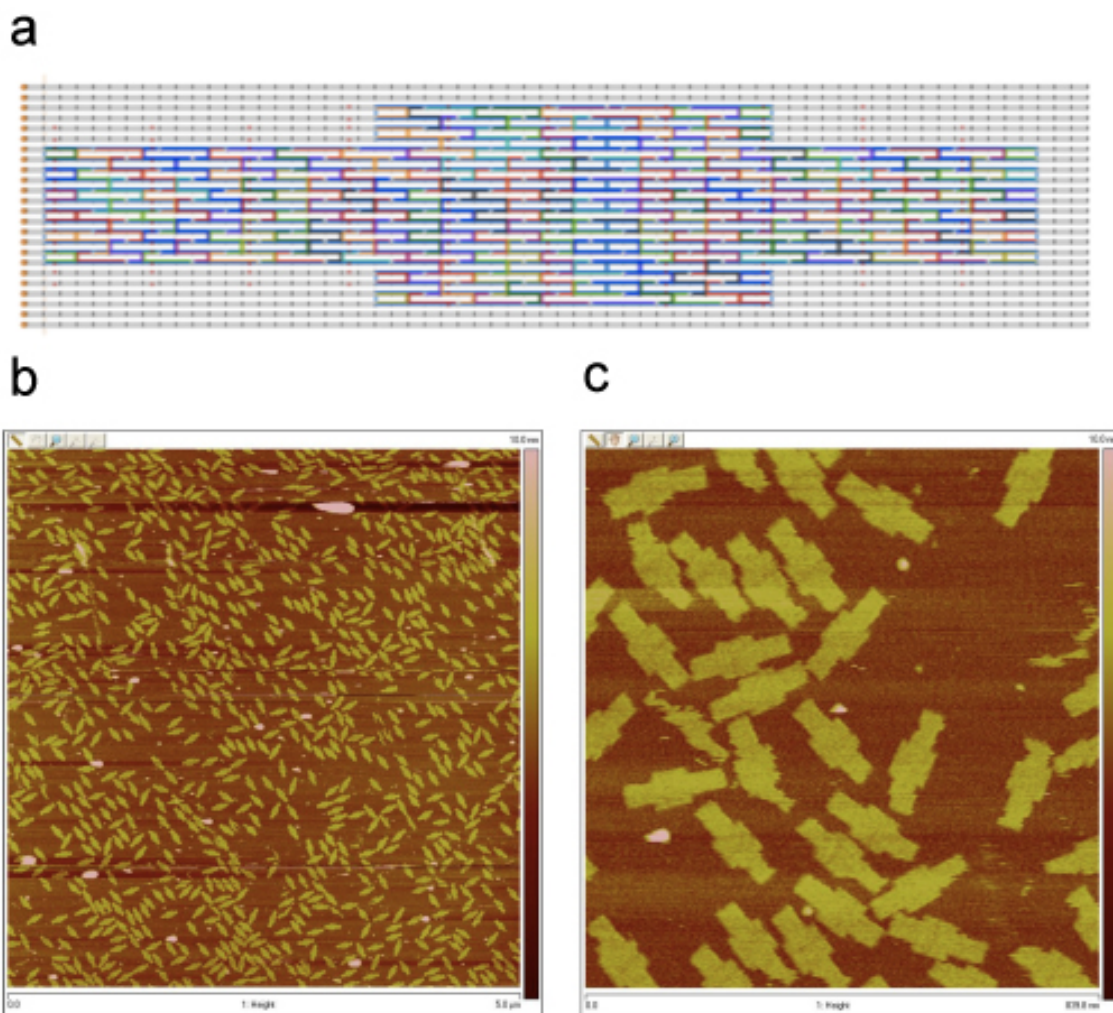


Figure S12 Design and AFM images of DNA origami scaffold. (a) Design of the DNA origami. Each color shows individual single stranded DNAs. The constructed DNA origami scaffold was examined by AFM. Scale: **(b)** 5.0 μm x 5.0 μm ; **(c)** 839.8 nm x 839.8 nm.

15 Design and preparation of gold covered DNA origami

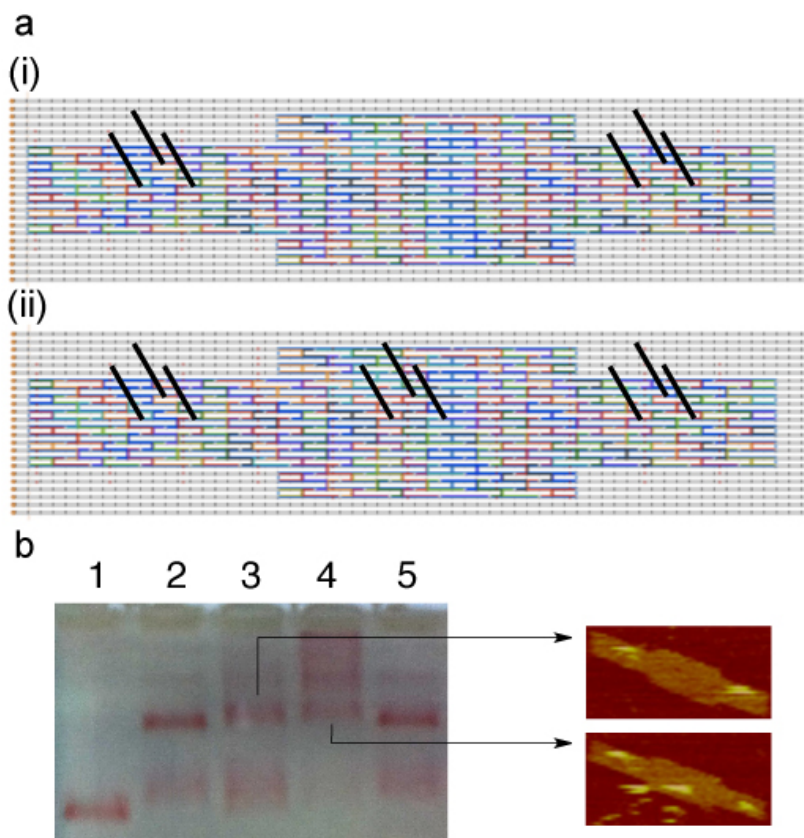


Figure S13 Design and preparation of gold nanoparticles-embedded DNA origami. (a) The design of DNA origami structures with two (i) and three (ii) binding sites for DNA-modified gold nanoparticles. (b) Agarose gel analysis and AFM images of the gold nanoparticles-embedded DNA origami. Annealed products of DNA origami with gold nanoparticles were loaded on 1% Sybr safe-stained agarose gel containing 10 mM MgCl₂ (running buffer TBE (0.5X), loading buffer 40% glycerol, 15 V/cm, 30 minutes, room temperature). Lane 1 contains 15 nm gold nanoparticles fully covered by DNA. Lane 2 contains DNA origami with one binding site and the DNA-modified gold nanoparticles. (origami:gold = 1:1) Lane 3 contains DNA origami with two binding sites and the DNA-modified gold nanoparticles (origami:gold = 1:2). Lane 4 contained DNA origami with three binding sites and the DNA-modified gold nanoparticles (origami:gold = 1:3). Lane 5 contains DNA origami with one binding site and the DNA-modified gold nanoparticle, same as lane 2. The selected bands were excised and purified for analysis using Freeze-squeeze column (Bio-Rad) at 4°C. 4 μl NiCl₂ (10 mM) was dropped on freshly cleaved mica. After 20 minutes, the surface was dried by nitrogen gas. 4 μl of the sample with DNA origami and gold nanoparticles was dropped on the pretreated substrate. Then the samples were scanned in TAE-Mg²⁺ (1X) buffer on AFM (Veeco Multimode with NanoScope V) in tapping mode with a SNL-10 tip (Bruker corporation). Scale: 100 nm x 200 nm.

17 References

1. Albrecht TR, Grütter P, Horne D, Rugar D (1991) Frequency modulation detection using high-Q cantilevers for enhanced force microscope sensitivity. *J Appl Phys* 69:668–673.
2. Arlett JL, Roukes ML (2010) Ultimate and practical limits of fluid-based mass detection with suspended microchannel resonators. *J Appl Phys* 108.
3. Cleland AN, Roukes ML (2002) Noise processes in nanomechanical resonators. *J Appl Phys* 92:2758–2769.
4. Dohn S, Svendsen W, Boisen A, Hansen O (2007) Mass and position determination of attached particles on cantilever based mass sensors. *Rev Sci Instrum* 78:103303–103303–3.
5. Van Der Pol E et al. (2010) Optical and non-optical methods for detection and characterization of microparticles and exosomes. *J Thromb Haemost* 8:2596–2607.